Title

Rechargeable Batteries from the Perspective of the Electron Spin

Journal

ACS Energy Letters, 5(12)

ISSN

2380-8195

Authors

Nguyen, Howie

Clément, Raphaële J

Publication Date

2020-12-11

DOI

10.1021/acsenergylett.0c02074

Peer reviewed

Rechargeable batteries from the perspective of the electron spin

Howie Nguyen,[1,2] Raphaële J. Clément*[1,2]

1. Materials Department, University of California, Santa Barbara, CA 93106-5050, United States.

2. Materials Research Laboratory, University of California, Santa Barbara, CA 93106-5121, United States.

AUTHOR INFORMATION

Corresponding Author

* rclement@ucsb.edu

ABSTRACT

Rechargeable batteries generate current through the transfer of electrons between paramagnetic and/or metallic electrode materials. Electron spin probes, such as electron paramagnetic resonance (EPR) and magnetometry, can therefore provide detailed insight into the underlying energy storage mechanisms. These techniques have been applied *ex situ*, and more recently *operando*, to both intercalation- and conversion-type batteries. After briefly reviewing the principles of EPR and magnetometry, this perspective provides a critical discussion of recent studies that leverage these tools to understand the local structure, defect chemistry and charge/discharge and failure mechanisms of rechargeable batteries. Challenges in data collection and interpretation are addressed and strategies to facilitate EPR spectral assignment and expand the scope of EPR and magnetometry studies of battery systems are suggested.

TOC GRAPHICS

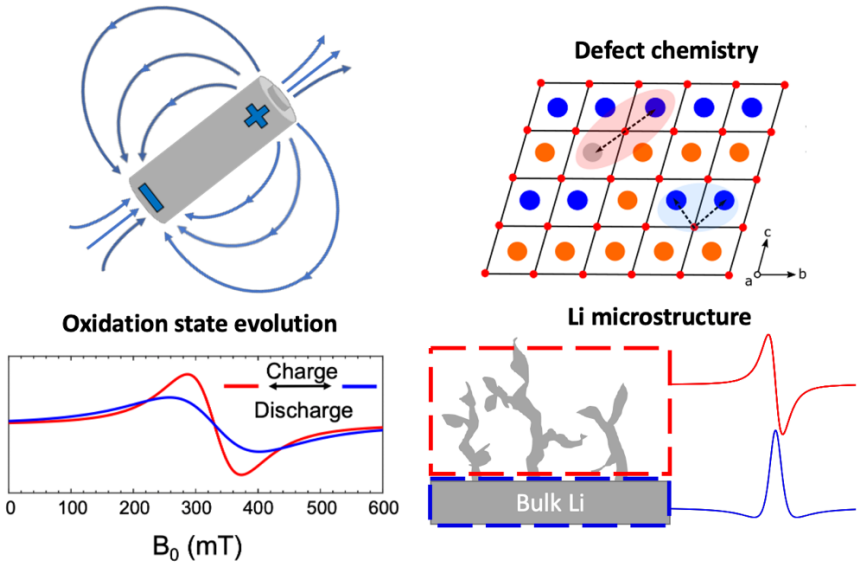

The 2019 Nobel prize honored John B. Goodenough, M. Stanley Whittingham, and Akira Yoshino for their contributions to the development of lithium (Li)–ion batteries. Ever since their pioneering work resulting in the first commercially viable Li-ion battery based on a $LiCoO_2$ (LCO) cathode and a graphitic anode, extensive efforts have been invested in energy storage research. The discovery of LCO is owed, in part, to Whittingham's seminal work on Li intercalation hosts[1] and Goodenough's substantial work on the magnetic and electronic behavior of transition metal oxides.[2–5] High electronic conductivity and the high oxidation potential of the Co^{3+}/Co^{4+} redox couple make LCO a rather good cathode material that is still in use today.[6] We, and many others, find inspiration in this example, which illustrates the interrelation between a material's magnetic and electronic properties and its performance as a battery electrode, and intimates the use of the electron spin as a probe of redox processes in electrochemical energy storage systems.[7] Two techniques are appropriate, electron paramagnetic resonance (EPR) and magnetometry, which interrogate the local environments of unpaired electrons, i.e., of open-shell species in the system, and possible long-range magnetic couplings. A focus on local structure and local redox properties, as obtained from a combination of these techniques, especially in the presence of defects or compositional inhomogeneities, is indispensable in order to realize higher energy density and structurally stable electrodes. As such, EPR and magnetometry have and will continue to make significant contributions to our understanding of the function of electrode materials and inform the design of next-generation chemistries.

Recent years have witnessed a strong push towards *operando* analysis of battery materials, with the development of electrochemical setups (sample holders, probes, etc.) for real-time X-ray absorption spectroscopy (XAS), X-ray diffraction (XRD), differential electrochemical mass spectrometry (DEMS), transmission electron microscopy (TEM), and nuclear magnetic resonance

(NMR) measurements.[8,9] Techniques based on *operando* monitoring of electron spins occupy a unique position in this gamut of techniques, yet are not as developed and widely used. In this perspective, we briefly review the technical background of *ex situ* and *operando* EPR and magnetometry and critically evaluate results from studies to date. We provide strategies for data disambiguation and interpretation and argue that these two complementary techniques should be used in conjunction. Finally, future opportunities for the application of EPR and magnetometry to battery research are discussed.

Electron transfer processes during electrochemical (charge-discharge) cycling of a battery result in the formation (or are enabled by the presence) of unpaired electrons in the bulk of the electrodes. In insulating or semiconducting electrode compounds comprising redox-active transition metal (TM) species, these unpaired electrons are localized in *d* orbitals and generally result in Curie-Weiss paramagnetism under normal operating conditions. Bulk metal electrodes, on the other hand, contain itinerant electrons and display Pauli paramagnetism. In both cases, magnetometry and EPR can be used to monitor electron transfer mechanisms in real time and are therefore ideal for full device analysis.

Magnetometry is the measurement of the magnetization (M) or magnetic susceptibility ($\chi = \frac{M}{H}$) of a sample as a function of applied magnetic field (H) or temperature (T). The evolution

of the room temperature magnetization M of the electrode with charge-discharge provides insight into the sequence of redox processes and into the formation of metallic phases.

The temperature-dependent magnetic susceptibility (χ) of Curie-Weiss paramagnets can be fitted to the Curie–Weiss law above the critical temperature (the Néel temperature for antiferromagnets and the Curie temperature for ferromagnets):

$$\chi = \frac{C}{T-\theta_{CW}}, \qquad (1)$$

where C is the material-dependent Curie constant, T is the temperature, and θ_{cw} is the Curie temperature. θ_{CW} is a measure of the strength of magnetic exchange interactions (J) mediated by open-shell TM centers with spin S, as described by the approximate mean field expression

$$\theta_{CW} = \frac{2}{3}\frac{S(S+1)zJ}{k_B}, \qquad (2)$$

where z is the number of interacting nearest-neighbor paramagnetic centers and k_B is Boltzmann's constant. A negative θ_{cw} signifies an overall antiferromagnetic system, while a positive θ_{cw} indicates a ferromagnetic material.

Magnetometry is a powerful tool for the study of conversion-type alkali-ion batteries, where alloying reactions between the alkali species and the electrode often result in the formation of ferro(i)magnetic nanoparticles. A characteristic hysteretic magnetization curve (M-H plot) for a ferromagnet is shown in Fig. 1a. Fig. 1b illustrates the hysteretic magnetization loop for three particle sizes. The corresponding plot of coercivity against nanoparticle size is shown in Fig. 1c.

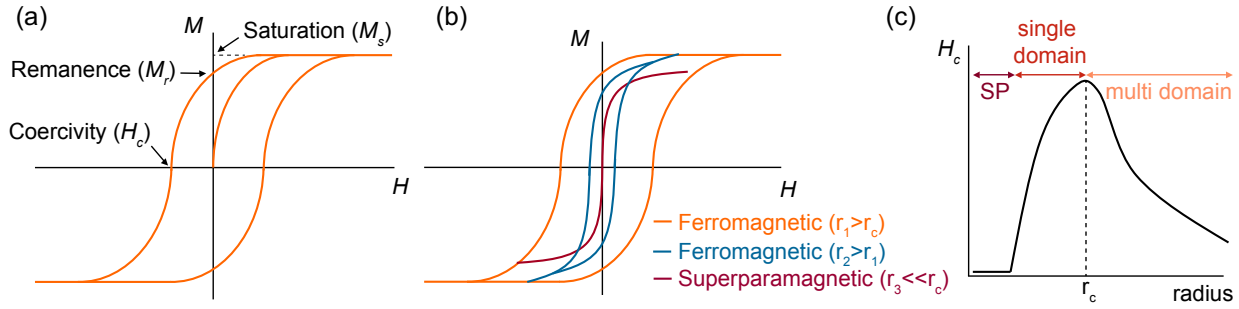

Figure 1. (a) Typical magnetization curve of a ferromagnet, featuring a saturation magnetization (M_s) at high applied H field and a magnetic hysteresis resulting in a remanent magnetization (M_r) as the field is switched off. A coercive field (H_c) is required to reduce the magnetization of the material to zero after being driven to saturation. Particle size effects on (b) the magnetic hysteresis loop and (c) the coercive field (H_c). For ferromagnetic materials, there exists a critical particle size r_c such that for particles with radius $r > r_c$, the hysteretic loop becomes narrower with increasing particle size, as shown with the orange and blue curves in (b). Conversely, for $r < r_c$, the hysteresis loop starts to narrow with decreasing particle size, until the superparamagnetic (SP) threshold is reached (r_3, dark red curve), when the magnetic response curve takes a sigmoidal shape but loses the hysteresis.

Superparamagnetism occurs in ferro(i)magnetic nanoparticles consisting of a single magnetic domain ($\emptyset \approx 3$ -50 nm). In this regime, the magnetization of each particle behaves as a single giant magnetic moment that randomly flips direction. The Néel relaxation time (τ_N) is the critical reorientational time. When the magnetization is measured over time intervals $\tau < \tau_N$, a blocked state occurs in which the measured magnetization is the instantaneous magnetization at the beginning of the measurement because there was no direction flip. In this state, the nanoparticles behave like normal paramagnets in an applied H field, but with a much higher susceptibility. When the measurement time $\tau \gg \tau_N$, a superparamagnetic state is observed whereby the net moment is zero due to the fluctuations in magnetization.

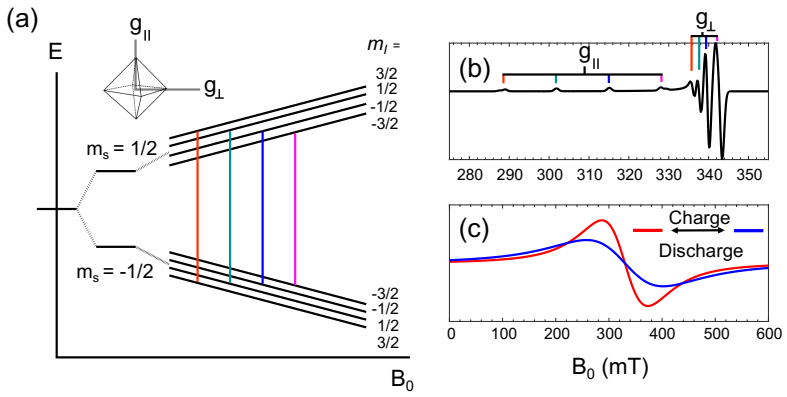

Figure 2. (a) Zeeman effect of an external magnetic field B_0 on the energy levels of a hypothetical two spin system (S=1/2; I=3/2) with axial symmetry, resulting in a parallel and perpendicular component of the **g**-tensor, $g_{\parallel}$ and $g_{\perp}$, respectively. (b) Simulated EPR spectrum of the isolated spin from (a) with hyperfine splitting. (c) Simulated EPR spectra of spin concentrated systems exhibiting different linewidths, *e.g.*, as observed for paramagnetic battery electrodes at different states of charge. Simulations were performed with EasySpin.[10]

EPR uses low energy microwave (MW) radiation to probe the energy levels of unpaired electron spins that are split in an external magnetic field through the Zeeman effect (Fig. 2a). Interactions between neighboring electron spins, or between electron and nuclear spins (hyperfine interactions), provide insight into the local environment and oxidation states of open-shell species in the sample. Notably, EPR is a site–specific technique, whereby each unique paramagnetic environment results in a distinct spectral signature. This resolution is advantageous over more standard characterization tools probing the long-range structure (e.g., XRD) or for which significant signal overlap complicates the deconvolution of contributions from redox-active species in various oxidation states (e.g., X-ray absorption near edge spectroscopy (XANES)). In EPR, the "fingerprint" of a specific unpaired electron spin environment takes the form of a **g**-tensor, which depends on the oxidation state, coordination geometry, and spin-orbit coupling properties of the paramagnetic species under consideration. Isotropic spin systems can be fully described using a single g-factor (a scalar value), while axial and rhombic systems require two ($g_{\parallel}$ and $g_{\perp}$) and three (g_x, g_y, and g_z) components, respectively. **g**-tensor components are experimentally

determined from the resonant field of the signal at a given MW frequency and/or from a fit of the signal lineshape. A simulated EPR spectrum corresponding to a spin S=1/2 open-shell species in an octahedral environment (local axial symmetry) and hyperfine coupled to a nuclear spin I=3/2 is shown in Fig. 2b. The EPR signal linewidth is affected by interactions with neighboring electron spins. In general, both through space dipole-dipole and through bond exchange interactions are present and have competing effects on the linewidth. Anisotropic dipole-dipole interactions, with an r^{-3} dependence, broaden the signal, while magnetic exchange (J) interactions lead to electron hopping between coupled sites and an average electron spin resonant frequency, effectively narrowing the EPR signal linewidth. Based on the phenomenological theory of Van Vleck[11] and Moriya[12], Stoyanova *et al*.[13] derived an expression for the peak-to-peak EPR signal linewidth, ΔH_{pp}:

$$\Delta H_{pp} = const * g^2\beta^2 \frac{\{S(S+1)\}^{3/2} z^{3/2}}{r^{-6}\theta_{CW}}, \quad (3)$$

where β is the Bohr magneton, z is the number of nearest-neighbor paramagnetic centers with spin S, and r is the distance between neighboring species. Compounds containing a high concentration of open-shell TM species, such as many battery electrodes, often lead to the formation of a percolating network of magnetic exchange couplings (Fig. 3a) and are in the exchange dominated regime, where the EPR signal is averaged between the different sites and effectively narrowed (Fig. 3b). Strong exchange interactions, such as those found in Ni^{2+}–Mn^{4+} systems, are expected to lead to significant narrowing of EPR resonances. Table 1 shows the relative magnetic exchange strengths for some transition metal combinations found in Li-ion batteries. The resulting exchange-narrowed EPR signal lineshapes are Lorentzian in the center and fall off rapidly on either side of the central frequency.[14] Due to dipole-dipole broadening effects, hyperfine splittings resulting from electron-nuclear spin interactions are scarcely resolved in EPR spectra, as shown in the simulation in Fig. 2c, and only an average g-factor can be obtained from a fit of the broad lineshape. Lastly,

the signal intensity is proportional to the number density of the corresponding local environment in the sample, and can be used (semi-)quantitatively. Variation of these three parameters (**g**-tensor, linewidth, and signal intensity) with temperature and battery state of charge (SOC) provide a comprehensive picture of the processes occurring in rechargeable batteries.

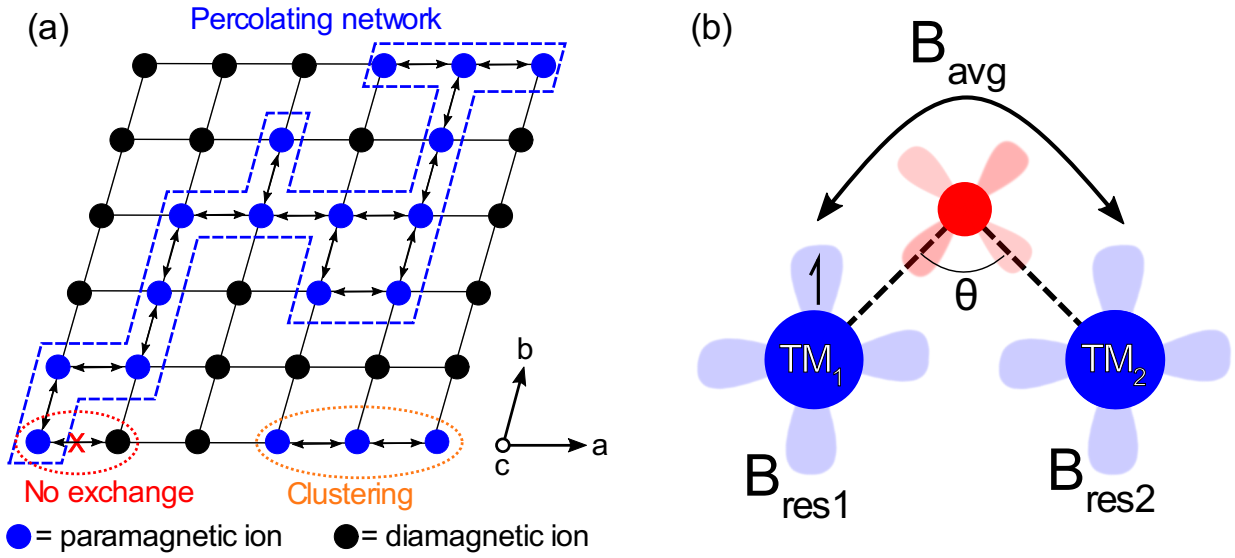

Figure 3. (a) Cation lattice of a paramagnetic battery electrode material. The formation of an extended network of magnetic exchange couplings between paramagnetic transition metal species in a matrix of diamagnetic cations leads to EPR signal narrowing. Yet, significant clustering of open-shell transition metals results in an increase in the threshold concentration for percolation. (b) Unpaired electrons at two different transition metal sites result in distinct resonant fields, B_{res1} and B_{res2}. In paramagnetic battery electrodes, a distribution of resonant fields leads to signal overlap and additional spectral broadening. However, in the presence of magnetic exchange interactions, unpaired electrons hop between neighboring transition metal sites and an average resonant field, B_{avg}, is obtained thereby narrowing the resonant signal. The degree of narrowing is dependent on the strength of the magnetic exchange interactions, i.e., on the transition metal identity, orbital filling and degree of orbital overlap (interaction angle). Most magnetic exchange interactions in transition metal oxides are superexchange couplings mediated by oxygen atoms.

Table 1. Magnitude of common magnetic superexchange interactions in lithium transition metal oxides.

Angle of interaction	**Transition metal identities**	**Relative Strength**	**Reference**
180°	Ni^{2+} – Ni^{2+}	Very strong	[15,16]

180°	Ni^{2+} – Mn^{4+}	strong	[15,16]
180°	Ni^{2+} – Co^{4+}	strong	[15]
180°	Ni^{2+} – Ni^{3+}	moderate	[15,16]
180°	Ni^{2+} – Co^{3+}	very weak	[15]
180°	Ni^{2+} – Ni^{3+}	moderate	[16]
90°	Ni^{2+} – Mn^{4+}	strong	[16]
90°	Ni^{2+} – Ni^{2+}	weak	[16]
90°	Mn^{4+} – Mn^{4+}	moderate	[16]

An important consideration for the investigation of battery devices with EPR is the existence of skin effects, which limit the penetration of MW radiation into metallic solids to a surface layer with a depth δ on the order of 100s of nanometers to micrometers at commonly used X-band frequencies (~9.5 GHz). The diffusion of conducting electrons in and out of the skin of the metal has a decisive effect on the shape and intensity of the observed resonance.[17,18] A Dysonian lineshape (a phase-shifted Lorentzian) is observed for metallic solids of thickness $D \gg \delta$, while a Lorentzian with no phase shift is observed for metallic structures with a thickness $D \approx \delta$. Hence, the EPR lineshape can provide clues as to the size of metallic structures formed during electrochemical cycling.

Magnetometry and EPR experiments can be performed *ex situ*, where the battery is disassembled after electrochemical cycling and electrode samples are extracted for analysis, or *operando*, where battery components are characterized as the cell is charged and discharged. *Ex situ* experiments are not time-constrained and can be carried out over a wide range of temperatures, magnetic fields and MW frequencies. *Ex situ* experiments conducted outside of the typical operating temperature range of battery devices can probe the magnetic ordering behavior of the

electrode material via EPR and magnetometry. Additionally, measurements at cryogenic temperatures result in enhanced EPR signal resolution and sensitivity, as well as longer signal lifetimes, while high field high frequency EPR experiments can resolve small g anisotropies and detect spin transitions with large energy splittings. Low temperature high frequency measurements are particularly useful to investigate non-Kramers integer spin TM centers, such as Ni^{2+} (S=1), exhibiting strong zero field splitting (ZFS) interactions that lift the degeneracy of the spin states in the absence of an external magnetic field. ZFS results in high energy EPR transitions that cannot be excited at X-band frequencies, as well as fast signal decay. High frequency measurements are restricted to *ex situ* studies as they generally require the material of interest to be loaded into a thin sample tube — tube diameters for Q-band (34 GHz) and W–band (94 GHz) experiments are 1.6 mm and 0.9 mm, respectively—. Unlike e*x situ* experiments, which entail the collection of many electrode samples at different states of charge to capture the behavior of a system, *operando* experiments can follow the evolution of a single electrode sample over the entire operational range of the electrochemical cell. *Operando* experiments also prevent sample damage that might occur on removal from the cell and are better suited for detecting transient species and monitoring reaction kinetics. Yet, despite the advantage of time-resolved data, the resolution of *operando* measurements is limited by the presence of other necessary battery components, such as current collectors, which introduce sharp and intense signals that overlap with the generally broad and low intensity signals from paramagnetic electrodes. Moreover, MW absorption by electronically conducting elements and high dielectric (aqueous and organic) electrolytes reduces the quality (Q) factor of the EPR resonator cavity, which indicates how efficiently it stores MW energy, and the overall sensitivity of the measurement.

The limited number of real-time EPR and magnetometry studies of secondary batteries to date is in part due to the challenges of *operando* cell development. EPR and magnetometry measurements involve the application of a strong magnetic field to the sample, requiring non-standard battery designs to minimize interactions with the electrical circuit, as well as shielding effects. For example, metal casings used in research-standard coin cells or Swagelok-type batteries must be replaced, while all the time ensuring that sufficient pressure is applied to the battery stack to maintain good electronic contact between individual components.

EPR studies of TM-based battery electrodes. *Paramagnetically-dilute electrodes* are advantageous for EPR studies as they enable the analysis of hyperfine splittings and the determination of **g**-tensor components, providing detailed information on the local structure. This has motivated several studies on diamagnetic LCO cathodes (containing low spin octahedral Co^{3+}) doped with paramagnetic TM species.[19–25] In such systems, large **g**-tensor anisotropies ($\Delta g = g_{\perp} - g_{\parallel}$) indicate distortions of the paramagnetic TMO_6 octahedra. For instance, Mladenov *et al.*[19] elegantly deduced the distribution of diamagnetic Mg^{2+} dopants in LCO from the **g**-anisotropy of inherent Ni^{3+} impurities. For systems containing more than one paramagnetic spin environment or species, differentiating between individual **g**-tensors is complicated by signal overlap at X-band frequencies. This limitation can be overcome with high field EPR, where larger Zeeman splittings increase signal resolution, as demonstrated by Stoyanova *et al.*[25] on a Ni/Mn co-doped LCO cathode. The authors identified Ni^{3+} and Mn^{4+} EPR signatures by matching their lineshapes to Ni^{3+}-doped LCO and Mn^{4+}-doped LCO, as shown in Fig. 4a, and used ZFS parameters extracted from fits of the EPR data to obtain trigonal distortion angles for MnO_6 octahedra. Generally, resolution enhancements obtained on paramagnetically-dilute electrodes do not persist upon electrochemical

cycling, as redox reactions taking place on charge-discharge result in a change in the magnetic character of TM species and in the formation of spin-concentrated systems.

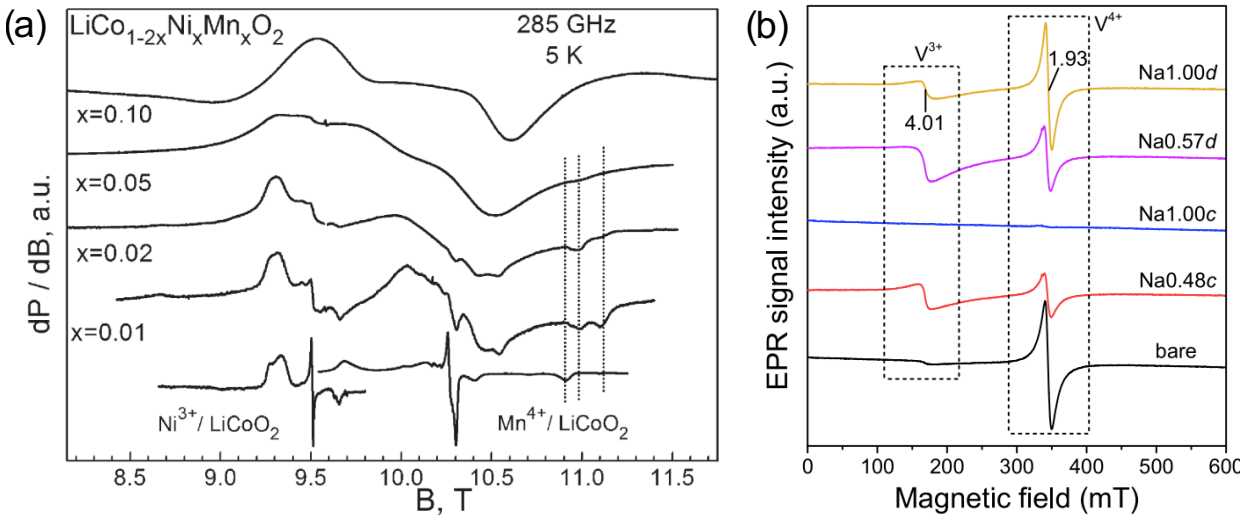

Figure 4. (a) High frequency (285 GHz) EPR spectra collected on a series of $LiCo_{1-2x}Ni_xMn_xO_2$ cathodes. As the paramagnetic ion concentration decreases (decrease in x), the fine structure of EPR signals is further resolved. At x=0.01, distinct Ni^{3+} and Mn^{4+} spectral signatures are identified by comparing with spectra obtained on Ni^{3+} doped $LiCoO_2$ and Mn^{4+} doped $LiCoO_2$. Fig. 4a reproduced with permission from reference 25. (b) *Ex situ* EPR spectra obtained on cycled $Na_{3-x}V_2^{3+/4+}(PO_4)_2O_{1.6}F_{0.4}$ cathode samples. The label above each spectrum indicates the state of charge, where 1.00c signifies 100% charged, and 1.00d signifies 100% discharged. V oxidation states were assigned based on the average g-factor of the two EPR signals. The evolution of V^{3+} and V^{4+} species was monitored through changes in the intensity of the two resonances, which provided evidence for the participation of V^{3+} in charge compensation processes. Fig. 4b reproduced with permission from reference 26.

In *paramagnetically concentrated systems*, EPR enables the detection of TM clusters through dipole-dipole and magnetic exchange interactions. Departure from a statistical distribution of paramagnetic species can be identified using eq. (3) and has been attributed to cation ordering in a variety of electrode systems, including layered and spinel transition metal oxides.[13,21,23,26,27] Further evidence for the formation of TM clusters can be obtained from the onset of exchange narrowing of the EPR signal. In systems featuring TM clustering, the onset of exchange narrowing occurs at a higher TM concentration than that expected based on a homogeneous distribution of paramagnetic species, as shown in Fig. 3. For example, it has been shown that exchange narrowing

begins at $x \geq 0.62$ for $LiNi_xCo_{1-x}O_2$, despite the $x = 0.5$ percolation threshold for layered TM oxide systems featuring a 2D triangular lattice, which highlights the tendency for Ni and Co species to cluster and prevent the formation of a continuous network of magnetically coupled Ni^{3+} ions.[23]

EPR measurements as a function of charge can provide key insights into redox and structural processes in electrode materials. For instance, gradual changes in the average g-factor are indicative of smooth changes in oxidation states, as occurs in solid solution reactions.[27] Alternatively, two-phase reactions can lead to the evolution of new EPR signals, such as in the V_2O_5 system studied by Gourier *et al*.[28] Upon discharge past the reversible limit, the authors detected the formation of an electrochemically-inactive phase with EPR, which provided an explanation for capacity loss in V_2O_5 cathodes. Another example is provided by Chao *et al*.[29], who studied mixed-valent $Na_3V_2^{3+/4+}(PO_4)_2O_{1.6}F_{0.4}$ cathodes at different states of charge using parallel-mode EPR, which enables the detection of integer spins such as V^{3+} (d^2, S=1), and found evidence for the oxidation of V^{3+} species previously thought to be redox-inactive in this system, as shown in Fig. 4b. More recently, researchers have claimed to detect oxidized oxygen species at high voltages in alkali rich cathodes, whose anomalous capacity is often attributed to anionic redox.[30,31]

Significant progress in *operando* EPR data processing and analysis has been made by Niemöller *et al*.[32] The introduction of a ruby reference into the *operando* EPR-electrochemical cell enabled them to correct for signal phase changes due to the cell's evolving impedance during electrochemical cycling, and a methodology was devised to monitor battery processes through a combined analysis of the

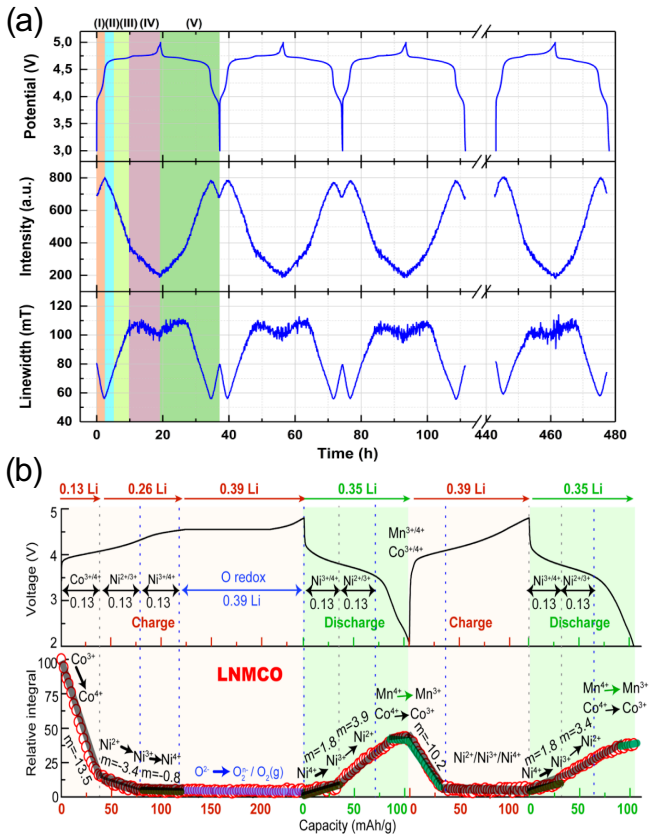

Figure 5. (a) *Operando* X-band EPR dataset collected on the $LiNi_{0.5}Mn_{1.5}O_{4-\delta}$ cathode, including the electrochemical profile (cell voltage vs. time, top panel) and corresponding changes to the cathode's EPR signal intensity (middle panel) and linewidth (bottom panel). Sequential redox events (I-V) are identified on the basis of the observed cell potential and of voltage regions corresponding to different rates of change (slope) of the EPR signal intensity and linewidth, as follows. Charge processes: (I) oxidation of residual Mn^{3+} in as-prepared O-deficient $LiNi_{0.5}Mn_{1.5}O_{4-\delta}$; (II) partial oxidation of Ni^{2+} to Ni^{3+} for those Ni species adjacent to the Mn^{3+} species in (I); (III) oxidation of the remaining Ni^{2+} species to Ni^{3+}; (IV) oxidation of Ni^{3+} species formed in (III) to Ni^{4+}. Discharge processes: (V) reduction events occur in the reverse order as compared to the charge processes listed above. Fig. 5a reproduced with permission from reference 32. Copyright 2018 American Institute of Physics. (b) *Operando* X-band EPR dataset collected on the $Li_{1.2}Ni_{0.13}Mn_{0.54}Co_{0.13}O_2$ cathode: electrochemical profile (top panel) and corresponding changes to the cathode's integrated EPR signal intensity (bottom panel). The large decrease in the EPR signal integral at the beginning of charge is assigned to the oxidation of Co^{3+} to Co^{4+}, followed by the oxidation of Ni^{2+} to Ni^{3+} and eventually Ni^{4+}. Although significant capacity is observed over the 4.5 V plateau in the electrochemical profile, no EPR signal is observed over this potential range, which the authors attribute to O redox processes. Fig. 5b reproduced from reference 33.

evolution of the signal intensity and linewidth as a function of charge. Within this scheme, changes in TM oxidation states are monitored through the degree of exchange narrowing, which not only depends on the concentration of paramagnetic centers, as previously seen, but also on the nature

and strength of magnetic couplings (J) between neighboring TM species. In transition metal oxides, these couplings are dominated by TM-O-TM superexchange interactions, which in turn depend on the electronic configuration of the coupled TM species, TM-TM distances and TM-O-TM bond angles and can, in simple cases, be predicted by the empirical Goodenough-Kanamori rules (Fig. 3b).[2,4,34,35] Using this methodology, Niemöller *et al*. identified sequential redox processes on charge-discharge of the spinel $LiNi_{0.5}Mn_{1.5}O_{4-\delta}$ cathode[32] on the basis of potential regions corresponding to different rates of change (slope) of the EPR signal intensity and linewidth, as shown in Fig. 5a. Notably, EPR's unique sensitivity to local redox processes allowed the resolution of two distinct Ni^{2+} oxidation processes, whereby Ni species closest to Mn^{3+} defects (and likely O^{2-} vacancies) in the as-prepared $LiNi_{0.5}Mn_{1.5}O_{4-\delta}$ cathode are oxidized first. These local processes are not discernable with electrochemical methods nor with XANES, yet provide crucial information on the impact of defects on the electrochemical properties of battery electrode materials.[32]

EPR data interpretation remains a complex task and, in the absence of corroborating evidence, incomplete or erroneous conclusions can be made. We note, for instance, the tendency of EPR studies on TM oxide cathodes to attribute charge compensation processes to oxygen species based on ambiguous observations and without further support from techniques that provide complementary insight into redox events (e.g., XANES, resonant inelastic X-ray scattering). An *operando* EPR study of the LCO cathode interpreted the absence of EPR signal during cycling between 3.0 and 4.2 V vs. Li^+/Li as evidence for purely O-based charge compensation processes and for the electrochemical inactivity of Co^{3+} species[36], even though prior work[37,38] has provided unequivocal evidence for $Co^{3+/4+}$ redox in this prototypical cathode material. Since Co^{4+} species have been observed at X-band frequencies and at room temperature in related materials[39], the absence of a detectable EPR signal as LCO is electrochemically cycled could result from the metal–insulator

transition reported upon delithation[40], as such processes are known to cause EPR signal decay.[41] A recent *operando* EPR study of the $Li_{1.2}Ni_{0.13}Mn_{0.54}Co_{0.13}O_2$ cathode rationalized the absence of EPR signal over the plateau at approximately 4.5 V vs. Li^+/Li in the electrochemical profile (see Fig. 5b) to the oxidation of O^{2-} species in the bulk.[33] While consistent with previous reports attributing the characteristic high voltage plateau of Li-excess layered $Li_{1+x}M_{1-x}O_2$ cathodes to O redox, this analysis is problematic in various ways. First, several experimental parameters, as well as the spin properties of the electrode material, are expected to evolve over the course of the *operando* measurement, and these have a direct impact on the integrated EPR signal intensity. Specifically, changes in the EPR signal lifetime, in the magnetic susceptibility of the cathode and in the Q factor of the resonator[42]. Second, no consensus has been reached on the exact charge compensation and structural processes at play in $Li_{1+x}M_{1-x}O_2$ cathodes, and mechanisms that do not involve O-based redox have been proposed.[43] Hence, if using the integrated EPR signal intensity as the sole metric for identifying redox processes, it is particularly important to eliminate confounding factors. For example, the evolution of the Q factor of the resonator can be accounted for by using a ruby reference[32], while changes in the magnetic properties and EPR signal lifetime of the cathode can be monitored by conducting *ex situ* magnetometry and low temperature EPR experiments. Moreover, the absence of EPR signal over the 4.5 V plateau is surprising given that both EPR-active Co^{4+} and Mn^{4+} have been reported at high voltage[44], and warrants further studies investigating the origin of signal disappearance. More generally, the absence of an EPR signal at X-band frequencies and at room temperature is an ambiguous result and should be treated with caution, since high energy electron spin transitions in, *e.g.*, paramagnetic species subject to ZFS cannot be excited and fast EPR signal decay can be an issue.

EPR studies of Li microstructures formed during electrochemical cycling. EPR experiments are uniquely positioned to monitor the evolution of metallic Li microstructures in Li-ion batteries. At X-band frequencies, skin effects limit the penetration of MWs to about one micron into bulk Li metal[31], such that a Lorentzian signal with zero phase shift is observed for Li structures with a sub-micron radius, while a Dysonian lineshape is obtained for thicker Li structures and smoothly plated Li, as shown in Fig. 6a. EPR methods have therefore been used to quantify (Fig. 6b)[33,45] and image mossy and dendritic Li (Fig. 6c).[46,47] Researchers have also taken advantage of conducting electron-nuclear spin interactions to identify Li microstructures using related electron-nuclear double resonance (ENDOR) methods[48] and, more recently, to hyperpolarize nuclei through DNP in the solid electrolyte interphase (SEI) forming at the surface of Li metal anodes[49]. Although Na is also EPR active[17], to the best of our knowledge, no EPR studies of Na metal anodes have been published to date.

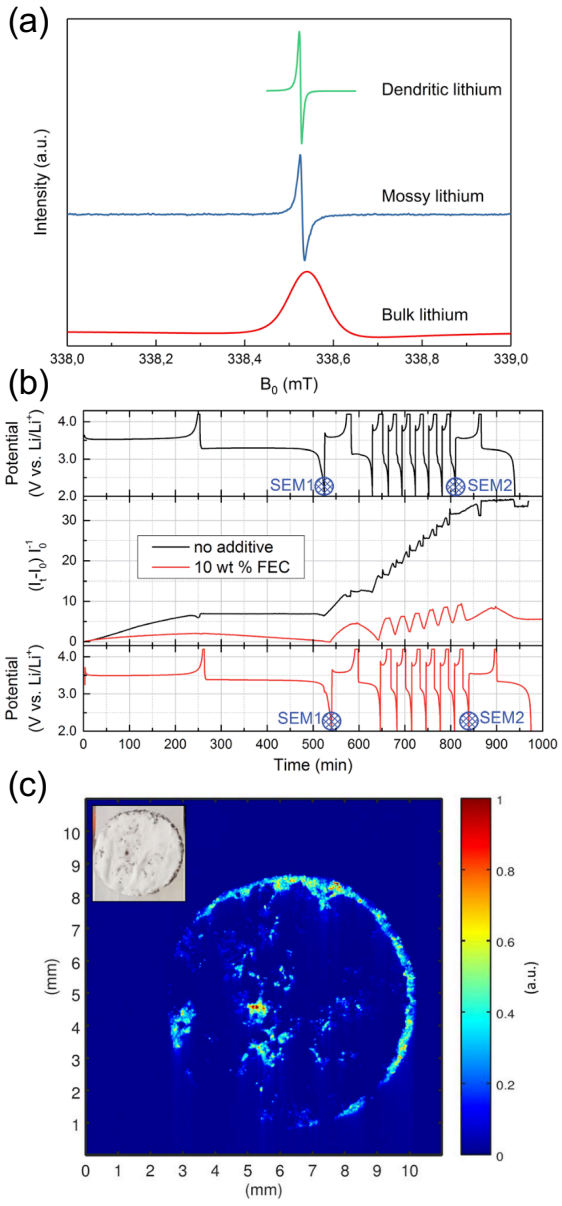

Figure 6. (a) Li metal microstructures that are much thicker than the skin depth δ = 1.1 μm at X-band frequencies lead to an EPR signal with a characteristic Dysonian lineshape (red spectrum). Microstructures that are on the same scale as δ (e.g. dendritic and mossy Li) lead to Lorentzian EPR signals with no phase shift (blue and green spectra). Fig. 6a reproduced from reference 47. (b) *Operando* quantification of dendritic Li with EPR. The top and bottom panels show two voltage profiles for a $LiFePO_4$/Li cell cycled with (red, bottom) and without (black, top) a fluoroethylene carbonate (FEC) additive in the electrolyte. The middle panel shows the normalized Li signal for both cells, which demonstrates the suppression of Li dendrites in FEC-containing cells. Fig. 6b reproduced from Wandt *et al.*[45] with permission from the Royal Society of Chemistry. (c) The Lorentzian Li signal for sub-micron Li structures is used to spatially map lithium dendrites in a Celgard separator extracted after electrochemical cycling. Dendrites are found to be agglomerated around the edges of the separator. Fig. 6c reproduced from Niemöller et al.[47] under the Creative Commons CC BY license.

EPR studies of beyond Li-ion batteries. EPR has been used to investigate Li–S and Li–O_2 batteries, where the energy storage mechanism results in the formation of radical species. Compared to paramagnetic TM species, S- and O-based radicals have longer relaxation times, resulting in higher sensitivity.[50] Additionally, these radicals are generally present in liquid phases, leading to motionally-narrowed signals and high resolution EPR spectra. Several *operando* or *ex situ* EPR studies of Li-S cells have monitored the concentration of long-lived S_3^- radicals in Li-S

cells, to gain insight into the polysulfide dissolution mechanisms resulting in rapid performance degradation.[51–53] Oxygen radicals that form in Li–O_2 batteries are, on the other hand, highly reactive, and EPR studies have employed spin traps, which are reagents added to the electrolyte solution that form stable EPR active adducts with radical oxygen species, to elucidate the mechanism of O-based reactions.[54,55]

Magnetometry studies of battery electrodes and devices. For electrode materials exhibiting Curie-Weiss behavior, the bulk magnetic susceptibility χ and Weiss constant θ_{cw} can provide insights into the local structure and the presence of defects[7,56]. An analysis of TM-O-TM magnetic exchange interactions is particularly useful to monitor structural rearrangements in layered transition metal oxide cathodes.[16,56,57] For instance, Li^+/Ni^{2+} antisite disorder in $Li_xNi_{0.5}Mn_{0.5}O_2$, whereby Li^+ and Ni^{2+} ions exchange positions in the layers, results in 180° interlayer TM-O-Ni^{2+} couplings that are stronger than 90° intralayer TM-O-TM interactions (Fig. 7a), and the large decrease in the low temperature bulk magnetic susceptibility across a series of cathode samples collected at the beginning of charge (Fig. 7b) has been attributed to preferential oxidation of TM ions involved in 180° interlayer exchange couplings.[16]

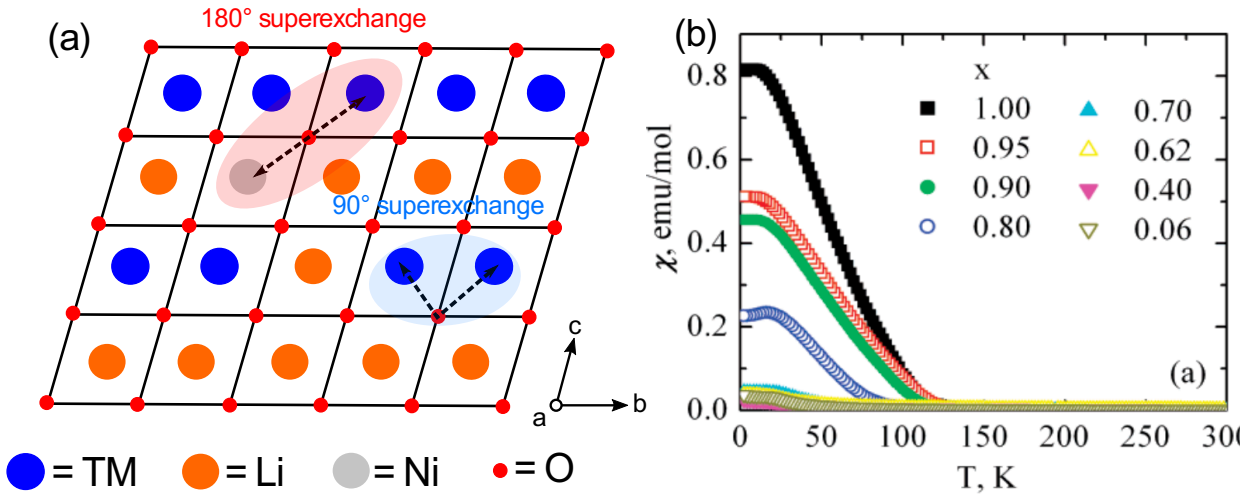

Figure 7. a) Li^+/Ni^{2+} antisite disorder in layered oxides leads to strong 180° interlayer TM-O-Ni^{2+} superexchange interactions (red) compared to the weaker 90° intralayer TM-O-TM superexchange interactions (blue). (b) *Ex situ* temperature-dependent bulk magnetic susceptibility measurements for $Li_xNi_{0.5}Mn_{0.5}O_2$ samples. A rapid loss of magnetization is observed in the range $1.0 \geq x \geq 0.7$, which suggests that TM species involved in the 180° interlayer couplings are oxidized first on charge. Fig. 7b reproduced from reference 16.

Beyond *ex situ* studies, very few *operando* magnetometry studies have been published to date. Unlike any other characterization technique, magnetometry can provide detailed insight into the nucleation and growth of ferromagnetic nanoparticles. Hence, it is perhaps unsurprising that the very first *operando* magnetometry study of a battery device was carried out on the conversion electrode $FeSb_2$ by Gershinsky *et al*.[58] The two-step conversion process on lithium insertion results in the formation of ferromagnetic Fe nanoparticles: (1) $FeSb_2 + 4\ Li \leftrightarrow Li_4FeSb_2$ followed by (2) $Li_4FeSb_2 + 2\ Li \leftrightarrow 2\ Li_3Sb + Fe$. The stepwise increase in the room temperature cell magnetization measured with each new lithiation process (Fig. 8a) was attributed to the steady growth of Fe nanoparticles with increasing cycle number[58] and a switch from superparamagnetic to ferromagnetic behavior as the individual particles reached a size greater than the critical radius (r_c, see Fig. 1). Notably, these results demonstrated that irreversible coarsening of metallic nanoparticles in conversion electrodes occurs even when the electrochemical profile remains relatively unchanged from one charge-discharge cycle to the next (Fig. 8a). *Ex situ* magnetic hysteresis measurements indicated that the conversion of $FeSb_2$ into separate Fe and Sb phases was already complete after the first lithiation and that Fe was no longer involved in the conversion process after the initial charge, leading the authors to propose a new reaction mechanism: $2\ Li_3Sb + Fe \leftrightarrow 2\ Sb + Fe + 6Li$.[58] Overall, this study proves that magnetometry can provide quantitative information on electrochemical processes when these involve the formation of a ferromagnetic phase, crystalline or amorphous, during cycling. More recent *operando* magnetometry studies of

conversion electrodes have investigated the Fe_3O_4 Li-ion system[59] and the electrochemical sodiation of $FeSb_2$.[60] Regarding intercalation electrodes, Würschum and coworkers have explored redox processes in layered oxides[61,62] and NASICON-type[63] cathodes by comparing changes in the magnetic susceptibility on charge-discharge to theoretically predicted changes based on various TM redox scenarios.

One particularly powerful application of magnetometry, which highlights the sensitivity and versatility of the technique, is high-throughput contactless battery diagnostics. Hu *et al*.[64] developed a susceptometry setup to spatially resolve weak induced magnetic fields in commercial Li-ion pouch cells. In a series of experiments on cells prepared and cycled under various conditions, the authors showed that the magnetic susceptibility, used as a proxy for state of charge, was inhomogeneously distributed across mechanically-deformed cells or when these were discharged beyond their rated voltage range (Fig. 8b).[64] This diagnostic technique is in principle scalable and could be adapted to screen larger commercial-type cell designs, such as those used in the electric car industry, in their target form factors. Importantly, this method could provide detailed spatial information about the battery state, and possible internal defects and damage, without compromising the cell.[64]

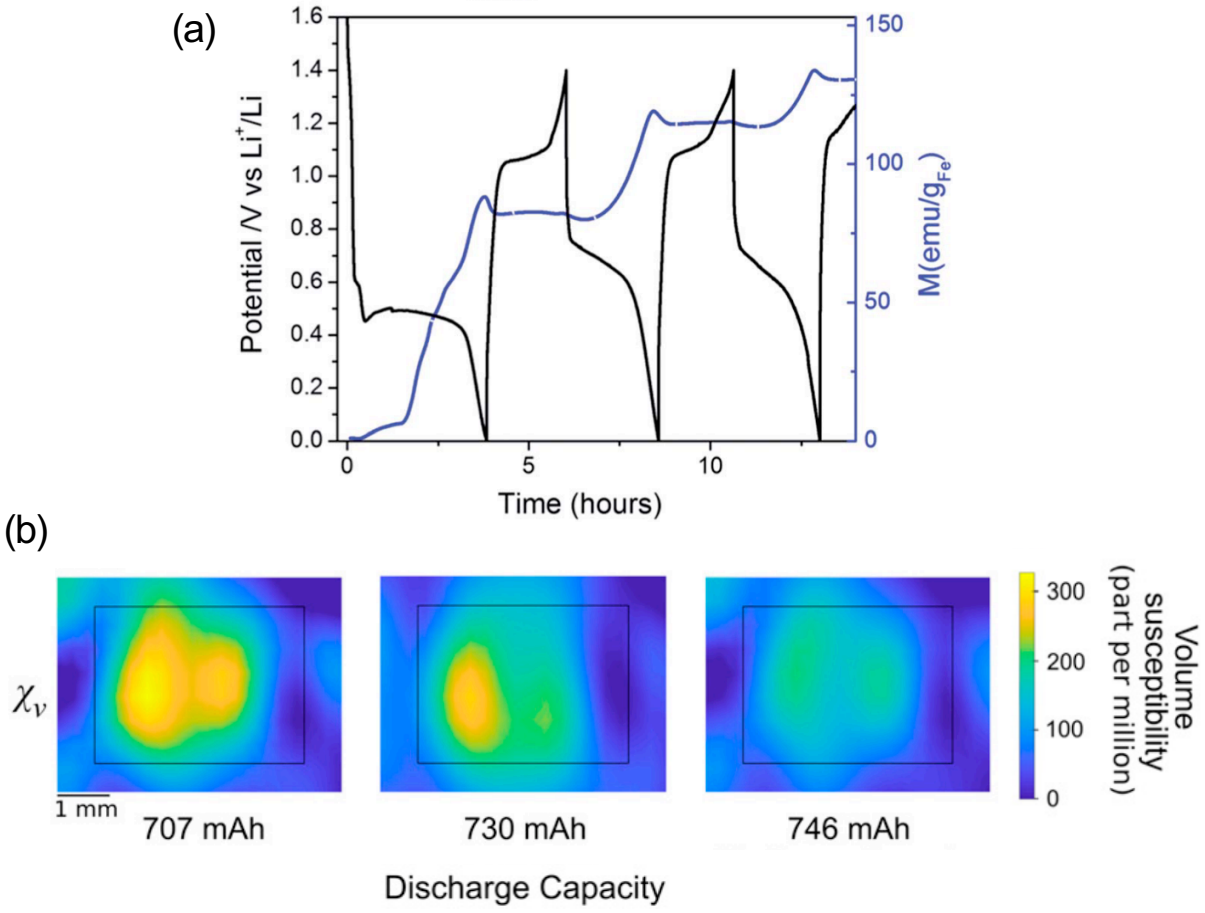

Figure 8. (a) *Operando* magnetometry data collected on the $FeSb_2$ conversion anode over several charge (lithiation)-discharge(delithiation) cycles. The electrochemical profile of the electrode is shown in black and the magnetic moment at 300 K in blue. The stepwise increase in magnetization with successive lithiation steps was attributed to coarsening of Fe nanoparticles formed in the initial charge process. Fig. 8a reproduced from reference 58 with permission from the Royal Society of Chemistry. (b) Magnetic susceptibility maps of a Li-ion pouch cell at different depths of discharge (discharge capacity shown below the plots). The pouch cell position is indicated by the black rectangular box with battery leads to the left of the box. The spatial distribution of the magnetic susceptibility decreases non uniformly from left to right, indicating heterogeneous reaction rates across the cell when the latter is discharged beyond its rated voltage range. Fig. 8b reproduced from reference 64.

While powerful tools for the study of battery processes, EPR and magnetometry results by themselves can be ambiguous. Their interpretation ought to be supported by corroborating evidence and by a robust theoretical framework, to prevent contradictory statements as to the nature of the electrochemical processes at play, as have been made for even prototypical electrode compounds such as LCO.[36–38,61]

As mentioned earlier, many factors can affect the EPR signal intensity and linebroadening, and an analysis based on such parameters needs to consider all factors that can affect the EPR response of the system. Importantly, the magnetization M (or χ) of a phase is directly related to its EPR signal intensity, while the strength and nature of the magnetic interactions (J) are related to the EPR signal linewidth. Hence, we argue that EPR and magnetometry should be used in combination, whereby a semi-quantitative analysis of the evolution of the EPR signal intensity and linewidth is compared against variations in the cell magnetization during cycling. Additionally, density functional theory (DFT) calculations of magnetic moments and exchange couplings on model compositions representative of charged/discharged states of the electrode material of interest can provide insight into the evolution of its EPR signal, M and χ with electrochemical cycling. This approach would allow, for example, to confirm the assignment of redox processes occurring at potentials where the EPR signal intensity/broadening and the magnetic susceptibility do not change significantly despite significant charge storage capacity being recorded, as observed in many Li-excess layered oxide cathodes.[33,36] *Ex situ* EPR experiments at high fields and high frequencies can excite spin transitions with large energy splittings and greatly enhance spectral resolution. Consequently, *operando* and *ex situ* EPR measurements are best employed in combination, *ex situ* spectra providing high resolution "snapshots" of time-resolved *operando* data and facilitating *operando* data interpretation. Furthermore, *ex situ* power saturation experiments, whereby the integrated EPR signal intensity is monitored as the MW power is gradually increased, are useful to distinguish between EPR resonances with similar g values. For instance, while oxygen radical signals have a g-factor close to the free electron g-value ($g_e = 2.00$),[46] polarization-type EPR signals (the oxygen radical) and conduction electron signals can easily be differentiated on the basis of their MW power relationship.[65] Finally, *ex situ* EPR measurements at cryogenic

temperatures enable the observation of short-lived or fast relaxing species, but one then needs to consider possible structural, charge-ordering or magnetic ordering transitions at low temperatures that might affect the EPR data.

The unparalleled sensitivity of EPR and magnetometry to changes in chemistry and electronic structure calls for a thorough characterization of electrode materials using a range of techniques, to avoid data misinterpretation. Specifically, the presence of defects or compositional inhomogeneities in the starting electrode material can greatly affect EPR and magnetometry results. For instance, special care should be taken to identify magnetic impurity phases that could obscure EPR and magnetometry data interpretation, *e.g.*, through *ex situ* variable-temperature magnetometry measurements. Neutron diffraction can be used to quantify antisite disorder in Ni^{2+}-containing layered oxides and provide clues as to the origin of the strong antiferromagnetic interactions observed upon Li^{+}/Ni^{2+} exchange between layers.[16] The oxidation states of TM species can be obtained through XANES measurements to correctly identify paramagnetic centers that contribute to the EPR signal, to the bulk magnetization and susceptibility at a given state of charge. While average oxidation states are generally deduced from XANES data, EPR can determine the relative distribution of oxidation states and provide clues as to the proximity of magnetically coupled TM species, as demonstrated by Niemöller *et al*.[32]

EPR and magnetometry are bound to play an important role in the discovery of next-generation battery chemistries and in our understanding of their working principles and failure mechanisms. We focus here on future opportunities for the study of all-solid-state, Li-S, Li-O_2 and conversion batteries, which are particularly attractive due to their high theoretical energy densities.

The ability to quantify dendritic or mossy Li has important implications for the study of solid electrolyte systems, which have been proposed to prevent dendrite growth on account of their high bulk modulus and to enable the safe use of Li metal in all-solid-state devices. Since dendrite growth has been observed in ceramic electrolytes at high cycling rates, real-time quantification of Li dendrites through *operando* EPR could shed light on the relative role of a high impedance interface, cycling rates and temperature on the formation of dendritic Li. EPR is also particularly well suited for the investigation of organic, Li-S and Li-O_2 batteries involving the formation/quenching of radical species on charge and discharge. Importantly, the very large theoretical capacities of Li-S and Li-O_2 systems are overshadowed by poorly reversible electrochemical processes that are not well understood. As of now, EPR has seldom been used to investigate the sources of irreversibility, leaving plenty of opportunities for future work. Finally, the application of advanced spectroscopic techniques is key to shed new light on electrochemical conversion mechanisms and to envisage new ways to improve the performance of conversion electrodes. EPR and magnetometry are uniquely suited for probing the growth of ferromagnetic particles in, *e.g.*, Fe-based conversion systems and for determining whether or not a conducting network is formed that enables reversible electron transfer processes during electrochemical cycling.[58,66,67] Notably, conversion reactions result in the formation of metastable phases that relax to more stable states with time,[58] warranting the use of *operando* EPR and magnetometry to study the kinetics of relaxation processes.

EPR and magnetometry offer a rare perspective on structural and redox processes from the standpoint of electron spins and magnetic interactions between redox-active species, holding promise for breakthroughs in our understanding of electrochemical energy storage devices. Significant advances have recently been made in *operando* EPR and magnetometry cell

development and data processing, opening new avenues for real-time investigation of local redox processes, phase transformations and structural rearrangements during charge-discharge. Data interpretation remains a complex task, which we believe could be greatly simplified through the concurrent use of *operando* EPR and magnetometry, as well as complementary scattering and X-ray absorption techniques to thoroughly characterize defects and compositional inhomogeneities that could affect EPR and magnetometry results. While EPR and magnetometry remain broadly unexplored by the battery community, they are uniquely positioned to provide atomic-level insight into the function of next-generation all-solid-state, Li-S and Li-O_2, as well as conversion battery chemistries.

AUTHOR INFORMATION

Corresponding author

rclement@ucsb.edu

Notes

The authors declare no competing financial interest.

ACKNOWLEDGEMENT

This work was partially supported by the Materials Research Science and Engineering Centers (MRSEC) Program of the National Science Foundation (NSF) under Award No. NSF DMR1720256 (IRG-2).

REFERENCES

(1) Whittingham, M. S.; Gamble, F. R. The Lithium Intercalates of the Transition Metal Dichalcogenides. *Mater. Res. Bull.* **1975**, *10* (5), 363–371. https://doi.org/10.1016/0025-5408(75)90006-9.

(2) Goodenough, J. B. Theory of the Role of Covalence in the Perovskite-Type Manganites [La,M(II)]MnO3. *Phys. Rev.* **1955**, *100* (2), 564–573. https://doi.org/10.1103/PhysRev.100.564.

(3) Goodenough, J. B.; Loeb, A. L. Theory of Ionic Ordering, Crystal Distortion, and Magnetic Exchange Due to Covalent Forces in Spinels. *Phys. Rev.* **1955**, *98* (2), 391–408. https://doi.org/10.1103/PhysRev.98.391.

(4) Goodenough, J. B. An Interpretation of the Magnetic Properties of the Perovskite-Type Mixed Crystals La1-XSrxCoO3-λ. *J. Phys. Chem. Solids* **1958**, *6* (2–3), 287–297. https://doi.org/10.1016/0022-3697(58)90107-0.

(5) Goodenough, J. B. On the Influence of 3d4 Ions on the Magnetic and Crystallographic Properties of Magnetic Oxides. *J. Phys. le Radium* **1959**, *20* (2–3), 155–159. https://doi.org/10.1051/jphysrad:01959002002-3015500.

(6) Mizushima, K.; Jones, P. C.; Wiseman, P. J.; Goodenough, J. B. LixCoO2: A New Cathode Material for Batteries of High Energy Density. **1980**, *15* (6), 783–789. https://doi.org/10.1016/0025-5408(80)90012-4.

(7) Chernova, N. A.; Nolis, G. M.; Omenya, F. O.; Zhou, H.; Li, Z.; Whittingham, M. S. What Can We Learn about Battery Materials from Their Magnetic Properties? *J. Mater. Chem.* **2011**, *21* (27), 9865–9875. https://doi.org/10.1039/c1jm00024a.

(8) Liu, D.; Shadike, Z.; Lin, R.; Qian, K.; Li, H.; Li, K.; Wang, S.; Yu, Q.; Liu, M.; Ganapathy, S.; Qin, X.; Yang, Q. H.; Wagemaker, M.; Kang, F.; Yang, X. Q.; Li, B. Review of Recent Development of In Situ/Operando Characterization Techniques for Lithium Battery Research. *Adv. Mater.* **2019**, *31* (28), 1–57. https://doi.org/10.1002/adma.201806620.

(9) Pecher, O.; Carretero-González, J.; Griffith, K. J.; Grey, C. P. Materials' Methods: NMR in Battery Research. *Chem. Mater.* **2016**, *29* (1), 213–242. https://doi.org/10.1021/acs.chemmater.6b03183.

(10) Stoll, S.; Schweiger, A. EasySpin, a Comprehensive Software Package for Spectral Simulation and Analysis in EPR. *J. Magn. Reson.* **2006**, *178* (1), 42–55. https://doi.org/10.1016/j.jmr.2005.08.013.

(11) Vleck van, J. H. The Dipolar Broadening of Magnetic Resonance Lines in Crystals. *Phys. Rev.* **1948**, *74* (9), 1168–1183. https://doi.org/doi.org/10.1103/PhysRev.74.1168.

(12) Moriya, T. Nuclear Magnetic Relaxation in Antiferromagnetics. *Progress of Theoretical Physics*. 1956, pp 23–44. https://doi.org/10.1103/PhysRev.101.1435.

(13) Stoyanova, R.; Gorova, M.; Zhecheva, E. EPR Monitoring of Mn4+ Distribution in Li4Mn5O12 Spinels. *J. Phys. Chem. Solids* **2000**, *61*, 615–620. https://doi.org/10.3724/SP.J.1077.2010.00626.

(14) Anderson, P.W.; Weiss, P. R. Exchange Narrowing in Paramagnetic Resonance. *Rev. Mod. Phys.* **1953**, *25* (1), 269–276. https://doi.org/10.1103/RevModPhys.25.269.

(15) Zheng, J.; Teng, G.; Xin, C.; Zhuo, Z.; Liu, J.; Li, Q.; Hu, Z.; Xu, M.; Yan, S.; Yang, W.;

Pan, F. Role of Superexchange Interaction on Tuning of Ni/Li Disordering in Layered Li(NixMnyCoz)O2. *J. Phys. Chem. Lett.* **2017**, *8* (22), 5537–5542. https://doi.org/10.1021/acs.jpclett.7b02498.

(16) Chernova, N. A.; Ma, M.; Xiao, J.; Whittingham, M. S.; Breger, J.; Grey, C. P. Layered LixNiyMnyCo1-2yO 2 Cathodes for Lithium Ion Batteries: Understanding Local Structure via Magnetic Properties. *Chem. Mater.* **2007**, *19* (19), 4682–4693. https://doi.org/10.1021/cm0708867.

(17) Feher, G.; Kip, A. F. Electron Spin Resonance Absorption in Metals. I. Experimental. *Phys. Rev.* **1955**, *98* (2), 337–348. https://doi.org/10.1103/PhysRev.98.337.

(18) Dyson, F. J. Electron Spin Resonance Absorption in Metals. II. Theory of Electron Diffusion and the Skin Effect. *Phys. Rev.* **1955**, *98* (2), 349–359. https://doi.org/10.1103/PhysRev.98.349.

(19) Mladenov, M.; Stoyanova, R.; Zhecheva, E.; Vassilev, S. Effect of Mg Doping and MgO-Surface Modification on the Cycling Stability of LiCoO2 Electrodes. *Electrochem. commun.* **2001**, *3* (8), 410–416. https://doi.org/10.1016/S1388-2481(01)00192-8.

(20) Mukai, K.; Aoki, Y.; Andreica, D.; Amato, A.; Watanabe, I.; Giblin, S. R.; Sugiyama, J. Thermally Activated Spin Fluctuations in Stoichiometric LiCoO 2 Clarified by Electron Paramagnetic Resonance and Muon-Spin Rotation and Relaxation Measurements. *Phys. Rev. B - Condens. Matter Mater. Phys.* **2014**, *89* (9). https://doi.org/10.1103/PhysRevB.89.094406.

(21) Zhecheva, E.; Stoyanova, R.; Shinova, E. EPR Analysis of the Local Structure of Ni3+ Ions in Ni-Based Electrode Materials Obtained under High-Pressure. *J. Mater. Sci.* **2007**, *42* (10), 3343–3348. https://doi.org/10.1007/s10853-006-0744-x.

(22) Stoyanova, R.; Zhecheva, E.; Alcántara, R.; Tirado, J. L. Changes in Local Ni/Mn Environment in Layered LiMgxNi0.5-XMn0.5O2($0 \leq x \leq 0.10$) after Electrochemical Extraction and Reinsertion of Lithium. *J. Mater. Chem.* **2006**, *16* (4), 359–369. https://doi.org/10.1039/b513243f.

(23) Stoyanova, R.; Zhecheva, E.; Alcántara, R.; Lavela, P.; Tirado, J. L. EPR Studies of Li1-x(NiyCo1-y) 1+xO2 Solid Solutions. *Solid State Commun.* **1997**, *102* (6), 457–462. https://doi.org/10.1016/S0038-1098(97)00008-2.

(24) Stoyanova, R.; Zhecheva, E.; Vassilev, S. Mn4+environment in Layered Li[Mg0.5-XNixMn0.5]O2oxides Monitored by EPR Spectroscopy. *J. Solid State Chem.* **2006**, *179* (2), 378–388. https://doi.org/10.1016/j.jssc.2005.10.038.

(25) Stoyanova, R.; Barra, A.-L.; Yoncheva, M.; Zhecheva, E.; Shinova, E.; Tzvetkova, P.; Simova, S. High-Frequency Electron Paramagnetic Resonance Analysis of the Oxidation State and Local Structure of Ni and Mn Ions in Ni,Mn-Codoped LiCoO ₂. *Inorg. Chem.* **2010**, *49* (4), 1932–1941. https://doi.org/10.1021/ic902351u.

(26) Stoyanova, R. K.; Zhecheva, E. N.; Gorova, M. Y. EPR Evidence on Short-Range Co/Mn Order in LiCoMnO4 Spinels. *J. Mater. Chem.* **2000**, *10* (6), 1377–1381. https://doi.org/10.1039/a909066e.

(27) Zhecheva, E.; Stoyanova, R.; Alcántara, R.; Lavela, P.; Tirado, J. L. EPR Studies of Li Deintercalation from LiCoMnO4 Spinel-Type Electrode Active Material. *J. Power Sources* **2006**, *159* (2), 1389–1394. https://doi.org/10.1016/j.jpowsour.2005.11.088.

(28) Gourier, D.; Tranchant, A.; Baffier, N.; Messina, R. EPR Study of Electrochemical Lithium Intercalation in V2O5 Cathodes. *Electrochim. Acta* **1992**, *37* (15), 2755–2764. https://doi.org/10.1016/0013-4686(92)85203-W.

(29) Li, C.; Shen, M.; Lou, X.; Hu, B. Unraveling the Redox Couples of VIII/VIV Mixed-Valent Na3V2(PO4)2O1.6F1.4 Cathode by Parallel-Mode EPR and in Situ/Ex Situ NMR. *J. Phys. Chem. C* **2018**, *122* (48), 27224–27232. https://doi.org/10.1021/acs.jpcc.8b09151.
(30) Geng, F.; Hu, B.; Li, C.; Zhao, C.; Lafon, O.; Trébosc, J.; Amoureux, J. P.; Shen, M.; Hu, B. Anionic Redox Reactions and Structural Degradation in a Cation-Disordered Rock-Salt Li1.2Ti0.4Mn0.4O2cathode Material Revealed by Solid-State NMR and EPR. *J. Mater. Chem. A* **2020**, *8* (32), 16515–16526. https://doi.org/10.1039/d0ta03358h.
(31) Li, C.; Zhao, C.; Hu, B.; Tong, W.; Shen, M.; Hu, B. Unraveling the Critical Role of Ti Substitution in P2-NaxLiyMn1- YO2 Cathodes for Highly Reversible Oxygen Redox Chemistry. *Chem. Mater.* **2020**, *32* (3), 1054–1063. https://doi.org/10.1021/acs.chemmater.9b03765.
(32) Niemöller, A.; Jakes, P.; Eurich, S.; Paulus, A.; Kungl, H.; Eichel, R.-A.; Granwehr, J. Monitoring Local Redox Processes in $LiNi_{0.5}Mn_{1.5}O_4$ Battery Cathode Material by *in Operando* EPR Spectroscopy. *J. Chem. Phys.* **2018**, *148* (1), 014705. https://doi.org/10.1063/1.5008251.
(33) Tang, M.; Dalzini, A.; Li, X.; Feng, X.; Chien, P. H.; Song, L.; Hu, Y. Y. Operando EPR for Simultaneous Monitoring of Anionic and Cationic Redox Processes in Li-Rich Metal Oxide Cathodes. *J. Phys. Chem. Lett.* **2017**, *8* (17), 4009–4016. https://doi.org/10.1021/acs.jpclett.7b01425.
(34) Goodenough, J. B. *Magnetism and the Chemical Bond*; Interscience- WIley: New York, 1963.
(35) Kanamori, J. Superexchange Interaction and Symmetry Properties of Electron Orbitals. *J. Phys. Chem. Solids* **1959**, *10* (2–3), 87–98. https://doi.org/10.1016/0022-3697(59)90061-7.
(36) Niemöller, A.; Jakes, P.; Eichel, R. A.; Granwehr, J. In Operando EPR Investigation of Redox Mechanisms in LiCoO 2. *Chem. Phys. Lett.* **2019**, *716* (December 2018), 231–236. https://doi.org/10.1016/j.cplett.2018.12.022.
(37) Hertz, J. T.; Huang, Q.; McQueen, T.; Klimczuk, T.; Bos, J. W. G.; Viciu, L.; Cava, R. J. Magnetism and Structure of Lix Co O2 and Comparison to Nax Co O2. *Phys. Rev. B* **2008**, *77* (7), 1–12. https://doi.org/10.1103/PhysRevB.77.075119.
(38) Yoon, W.-S.; Lee, K.-K.; Kim, K.-B. Structural and Electrochemical Properties of LiAl[Sub y]Co[Sub 1−y]O[Sub 2] Cathode for Li Rechargeable Batteries. *J. Electrochem. Soc.* **2000**, *147* (6), 2023. https://doi.org/10.1149/1.1393479.
(39) Carretta, P.; Mariani, M.; Azzoni, C. B.; Mozzati, M. C.; Bradarić, I.; Savić, I.; Feher, A.; Šebek, J. Mesoscopic Phase Separation in Na x CoO 2 (0.65≤x≤0.75). *Phys. Rev. B - Condens. Matter Mater. Phys.* **2004**, *70* (2), 1–9. https://doi.org/10.1103/PhysRevB.70.024409.
(40) Ménétrier, M.; Saadoune, I.; Levasseur, S.; Delmas, C. The Insulator-Metal Transition upon Lithium Deintercalation from LiCoO2: Electronic Properties and 7Li NMR Study. *J. Mater. Chem.* **1999**, *9* (5), 1135–1140. https://doi.org/10.1039/a900016j.
(41) Schlenker, C.; Ahmed, S.; Buder, R.; Gourmala, M. Metal-Insulator Transitions and Phase Diagram of (Ti1-XV x)4O7: Electrical, Calorimetric, Magnetic and EPR Studies. *J. Phys. C Solid State Phys.* **1979**, *12* (17), 3503–3521. https://doi.org/10.1088/0022-3719/12/17/021.
(42) Eaton, G. R.; Eaton, S. S.; Barr, D. P.; Weber, R. T. *Quantitative EPR*; Springer-Verlag/Wien, 2010.

(43) Radin, M. D.; Vinckeviciute, J.; Seshadri, R.; Ven, A. Van Der. Mn Oxidation as the Origin of the Anomalous Capacity of Mn - Containing Li - Excess Cathode Materials. *Nat. Energy* **2019**, *4* (August), 19–21. https://doi.org/10.1038/s41560-019-0439-6.
(44) Koga, H.; Croguennec, L.; Ménétrier, M.; Mannessiez, P.; Weill, F.; Delmas, C. Different Oxygen Redox Participation for Bulk and Surface: A Possible Global Explanation for the Cycling Mechanism of Li1.20Mn0.54Co0.13Ni0.13O2. *J. Power Sources* **2013**, *236*, 250–258. https://doi.org/10.1016/j.jpowsour.2013.02.075.
(45) Wandt, J.; Marino, C.; Gasteiger, H. A.; Jakes, P.; Eichel, R. A.; Granwehr, J. Operando Electron Paramagnetic Resonance Spectroscopy-Formation of Mossy Lithium on Lithium Anodes during Charge-Discharge Cycling. *Energy Environ. Sci.* **2015**, *8* (4), 1358–1367. https://doi.org/10.1039/c4ee02730b.
(46) Sathiya, M.; Leriche, J. B.; Salager, E.; Gourier, D.; Tarascon, J. M.; Vezin, H. Electron Paramagnetic Resonance Imaging for Real-Time Monitoring of Li-Ion Batteries. *Nat. Commun.* **2015**, *6*, 1–7. https://doi.org/10.1038/ncomms7276.
(47) Niemöller, A.; Jakes, P.; Eichel, R. A.; Granwehr, J. EPR Imaging of Metallic Lithium and Its Application to Dendrite Localisation in Battery Separators. *Sci. Rep.* **2018**, *8* (1), 1–7. https://doi.org/10.1038/s41598-018-32112-y.
(48) Vigreux, C.; Loiseau, P.; Binet, L.; Gourier, D. Anomalous Metallic Lithium Phases: Identification by ESR, ENDOR, and the Bistable Overhauser Effect. *Phys. Rev. B - Condens. Matter Mater. Phys.* **2000**, *61* (13), 8759–8770. https://doi.org/10.1103/PhysRevB.61.8759.
(49) Hope, M. A.; Rinkel, B. L. D.; Gunnarsdóttir, A. B.; Märker, K.; Menkin, S.; Paul, S.; Sergeyev, I. V.; Grey, C. P. Selective NMR Observation of the SEI–Metal Interface by Dynamic Nuclear Polarisation from Lithium Metal. *Nat. Commun.* **2020**, *11* (1), 2224. https://doi.org/10.1038/s41467-020-16114-x.
(50) Berliner, L. J.; Eaton, G. R.; Eaton, S. S. *Distance Measurements in Biological Systems by EPR*; 2002; Vol. 19. https://doi.org/10.1007/b111467.
(51) Wang, Q.; Zheng, J.; Walter, E.; Pan, H.; Lv, D.; Zuo, P.; Chen, H.; Deng, Z. D.; Liaw, B. Y.; Yu, X.; Yang, X.; Zhang, J.-G.; Liu, J.; Xiao, J. Direct Observation of Sulfur Radicals as Reaction Media in Lithium Sulfur Batteries. *J. Electrochem. Soc.* **2015**, *162* (3), A474–A478. https://doi.org/10.1149/2.0851503jes.
(52) Wujcik, K. H.; Wang, D. R.; Raghunathan, A.; Drake, M.; Pascal, T. A.; Prendergast, D.; Balsara, N. P. Lithium Polysulfide Radical Anions in Ether-Based Solvents. *J. Phys. Chem. C* **2016**, *120* (33), 18403–18410. https://doi.org/10.1021/acs.jpcc.6b04264.
(53) Barchasz, C.; Molton, F.; Duboc, C.; Leprêtre, J. C.; Patoux, S.; Alloin, F. Lithium/Sulfur Cell Discharge Mechanism: An Original Approach for Intermediate Species Identification. *Anal. Chem.* **2012**, *84* (9), 3973–3980. https://doi.org/10.1021/ac2032244.
(54) Nava, M. J.; Britt, D. R.; Nocera, D. G.; Cummins, C. C.; Lopez, N.; Wu, G.; Chow, G. K.; Zhang, S. On the Incompatibility of Lithium–O 2 Battery Technology with CO 2 . *Chem. Sci.* **2017**, *8* (9), 6117–6122. https://doi.org/10.1039/c7sc01230f.
(55) Cao, R.; Walter, E. D.; Xu, W.; Nasybulin, E. N.; Bhattacharya, P.; Bowden, M. E.; Engelhard, M. H.; Zhang, J. G. The Mechanisms of Oxygen Reduction and Evolution Reactions in Nonaqueous Lithium–Oxygen Batteries. *ChemSusChem* **2014**, *7* (9), 2436–2440. https://doi.org/10.1002/cssc.201402315.
(56) Dahbi, M.; Wikberg, J. M.; Saadoune, I.; Gustafsson, T.; Svedlindh, P.; Edström, K. Electrochemical Behavior of LiNi1-y-ZCoyMn ZO2 Probed through Structural and

Magnetic Properties. *J. Appl. Phys.* **2012**, *111* (2). https://doi.org/10.1063/1.3676434.
(57) Mohanty, D.; Gabrisch, H. Microstructural Investigation of Li XNi 1/3Mn 1/3Co 1/3O 2 (x ≤ 1) and Its Aged Products via Magnetic and Diffraction Study. *J. Power Sources* **2012**, *220*, 405–412. https://doi.org/10.1016/j.jpowsour.2012.08.005.
(58) Gershinsky, G.; Bar, E.; Monconduit, L.; Zitoun, D. Operando Electron Magnetic Measurements of Li-Ion Batteries. *Energy Environ. Sci.* **2014**, *7* (6), 2012–2016. https://doi.org/10.1039/c4ee00490f.
(59) Li, Q.; Li, H.; Xia, Q.; Hu, Z.; Zhu, Y.; Yan, S.; Ge, C.; Zhang, Q.; Wang, X.; Shang, X.; Fan, S.; Long, Y.; Gu, L.; Miao, G.; Yu, G.; Moodera, J. S. Extra Storage Capacity in Transition Metal Oxide Lithium-Ion Batteries Revealed by in Situ Magnetometry. *Nat. Mater.* https://doi.org/10.1038/s41563-020-0756-y.
(60) Fehse, M.; Bessas, D.; Darwiche, A.; Mahmoud, A.; Rahamim, G.; La Fontaine, C.; Hermann, R. P.; Zitoun, D.; Monconduit, L.; Stievano, L.; Sougrati, M. T. The Electrochemical Sodiation of FeSb 2 : New Insights from Operando 57 Fe Synchrotron Mössbauer and X-Ray Absorption Spectroscopy . *Batter. Supercaps* **2019**, *2* (1), 66–73. https://doi.org/10.1002/batt.201800075.
(61) Topolovec, S.; Kren, H.; Klinser, G.; Koller, S.; Krenn, H.; Würschum, R. Operando Magnetometry on LixCoO2 during Charging/Discharging. *J. Solid State Electrochem.* **2016**, *20* (5), 1491–1496. https://doi.org/10.1007/s10008-015-3110-6.
(62) Klinser, G.; Topolovec, S.; Kren, H.; Koller, S.; Goessler, W.; Krenn, H.; Würschum, R. Continuous Monitoring of the Bulk Oxidation States in Li x Ni 1 / 3 Mn 1 / 3 Co 1 / 3 O 2 during Charging and Discharging. *Appl. Phys. Lett.* **2016**, *109* (21), 0–4. https://doi.org/10.1063/1.4968547.
(63) Klinser, G.; Zettl, R.; Wilkening, M.; Krenn, H.; Hanzu, I.; Würschum, R. Redox Processes in Sodium Vanadium Phosphate Cathodes – Insights from Operando Magnetometry . *Phys. Chem. Chem. Phys.* **2019**, *21* (36), 20151–20155. https://doi.org/10.1039/c9cp04045e.
(64) Hu, Y.; Iwata, G. Z.; Mohammadi, M.; Silletta, E. V.; Wickenbrock, A.; Blanchard, J. W.; Budker, D.; Jerschow, A. Sensitive Magnetometry Reveals Inhomogeneities in Charge Storage and Weak Transient Internal Currents in Li-Ion Cells. *Proc. Natl. Acad. Sci. U. S. A.* **2020**, *117* (20), 10667–10672. https://doi.org/10.1073/pnas.1917172117.
(65) Wilamowski, Z.; Solnica, M.; Michaluk, E.; Havlicek, M.; Jantsch, W. EPR Line Shape and Magnetometry - Chances and Pitfalls. *Semicond. Sci. Technol.* **2011**, *26* (6). https://doi.org/10.1088/0268-1242/26/6/064009.
(66) Nwokeke, U. G.; Alcántara, R.; Tirado, J. L.; Stoyanova, R.; Yoncheva, M.; Zhecheva, E. Electron Paramagnetic Resonance, X-Ray Diffraction, Mössbauer Spectroscopy, and Electrochemical Studies on Nanocrystalline FeSn2 Obtained by Reduction of Salts in Tetraethylene Glycol. *Chem. Mater.* **2010**, *22* (7), 2268–2275. https://doi.org/10.1021/cm902898k.
(67) Dong, Z.; Wang, Q.; Zhang, R.; Chernova, N. A.; Omenya, F.; Ji, D.; Whittingham, M. S. Reaction Mechanism of the Sn2Fe Anode in Lithium-Ion Batteries. *ACS Omega* **2019**, *4* (27), 22345–22355. https://doi.org/10.1021/acsomega.9b02417.